Contents lists available at ScienceDirect

Journal of the European Ceramic Society

journal homepage: www.elsevier.com/locate/jeurceramsoc

Role of iron-rich clays on sintering of porcelain stoneware tiles

L. Nodari [a], S. Conte [b,*], L. Casini [c], M. Sisti [c], R. Fantini [c], A.F. Gualtieri [c], C. Molinari [b],
C. Zanelli [b], D. Giordano [b,d], M. Dondi [b], R. Arletti [c]

[a] *CNR-ICMATE, corso Stati Uniti 4, 35127 Padova, Italy*
[b] *CNR-ISSMC, via Granarolo 64, 48018 Faenza, Italy*
[c] *Dipartimento di Scienze Chimiche e Geologiche, University of Modena and Reggio Emilia, via G. Campi, 103, 41125 Modena*
[d] *Dipartimento di Scienze della Terra, University of Torino, via Verdi 8, 10124 Torino*

A B S T R A C T

Porcelain stoneware traditionally contains low Fe_2O_3 (<1 wt%), limiting research on iron's effects beyond coloration to date. However, recent changes in the supply chain induced a shift towards resource efficiency and circular economy, which led to body formulations with Fe_2O_3 up to 2.5 wt%. This study investigates the impact of iron-rich clays on the firing behaviour of porcelain stoneware, focusing on sintering processes, Fe speciation, and physical properties of the vitreous phase. Results show that red clays influence vitrification paths and maximum densification temperature, as well as composition and properties of the melt. This occurs not only because the relatively high iron percentage (up to 1.7 wt%), but for a set of factors, like the overall mineralogical and chemical composition of batches. Iron turns to be crucial for the stability of ceramic bodies at high temperatures, since Fe^{3+} can partially reduce to Fe^{2+}, releasing gases and contributing to bloating phenomena.

1. Introduction

Porcelain stoneware classically consists of a batch with low iron content, typically below 1 wt% by weight [1,2]. Therefore, the interest in understanding the effect of iron on the firing behaviour and performance of finished products has long been very little or at most limited to the colouring of the fired material [3–5]. Recently, however, the ceramic industry has had to develop new body formulations with a significantly higher iron content than the typical values, i.e. up to 2.5 wt% [6,7]. This is in response to changes in the supply chain and the growing pressure for greater resource efficiency and the transition to a circular economy [7–9].

Little is known about the implications that higher contents of iron oxide may have on the technological behaviour of porcelain stoneware batches, especially during firing. The knowledge in both scientific literature and industrial practice basically refer to red stoneware, whose body has iron oxide contents in the 4–8 wt% range [10–13]. However, these batches have been designed for firing schedules, degrees of vitrification, and tile dimensions very different from those of current porcelain stoneware production [14]. The main concern in firing red stoneware regarded black core and bloating, which seem to be linked to iron redox reactions that occur during firing [15,16]. Up to now, some

technological features have not been considered for red stoneware, such as the degree of densification and dimensional stability at high temperature, which are important for porcelain stoneware tiles and slabs [17,18]. Moreover, as far as we know, data on chemical composition and physical properties of the liquid phase in red stoneware have never been published.

The technological feasibility of porcelain stoneware manufacture with iron contents well above classical compositions has been recently assessed [6,19,20]. These studies demonstrated that ceramic tiles with physical properties conforming to standard requirements (BIa Group, ISO 13006) can be obtained, even if the colour of the fired bodies is much darker than that of classic whiteware, of course. What is not yet known, however, is the role of iron in the vitrification paths and, therefore, on chemical composition and physical properties of the liquid phase formed at high temperature in porcelain stoneware. Indeed, both shear viscosity and surface tension of the melt influence particularly kinetics and efficiency of densification in tiles largely constituted by aluminosilicate glass [21,22].

Therefore, the goal of this study is to shed light on the effect of relatively high amounts of iron oxide, provided by red clays, on sintering of porcelain stoneware tiles. Emphasis is on Fe speciation as well as on physical properties and pseudostructural features of the vitreous phase.

---

2. Background: iron in aluminosilicate melts and glasses

Porcelain stoneware typically consists of about 60–70 wt% of vitreous phase, which has a peraluminous chemical composition, rather rich in silica, where Na prevails over K, Ca, and Mg [21,23,24]. Much knowledge is available in the literature on compositions of aluminosilicate melts and glasses, concerning the Fe^{2+}/Fe^{3+} ratio as a function of temperature, oxygen fugacity, and melt composition [25–33]. In addition, the structural role of ferrous and ferric iron in aluminosilicate melts has been investigated in depth [30,34–43]. The effect of iron on viscosity and activation energy of viscous flow has been the object of several experimental studies and debates, as well [44–53].

The literature data suggest that the Fe^{3+}/Fe_{tot} ratio decreases with increasing temperature (Figure S1, supplementary material) and decreasing oxygen fugacity [26,30,31]. Nevertheless, at the maximum temperature (around 1200 °C) and oxygen fugacity of roller kilns used for porcelain stoneware firing (slightly below that of air), Fe^{3+} is expected to be more abundant than Fe^{2+} in the $NaAlSi_3O_8$ melt [30,54]. In the same system, however, at low iron concentrations – like those usually found in porcelain stoneware, with a silica plus alumina content normally larger than 70 wt% – Fe^{2+} can prevail over Fe^{3+} [36].

There is a general agreement on the structural role of iron, which for Fe^{3+} is largely glass network former (predominant tetrahedral coordination, charge compensated by alkaline and alkaline-earth cations) while for Fe^{2+} it is essentially glass network modifier with prevalent octahedral coordination [27,34,40]. Nevertheless, a range of coordination numbers and oxygen polyhedral distortions is probably a common condition [28,30,36,41]. In the case of silica-rich peraluminous melts [55], characteristic of porcelain stoneware, a competition between Al^{3+} and Fe^{3+} for charge compensation will occur. In this case, Fe^{3+} will likely be partitioned also in four-fold and five-fold coordinations (i.e., $^{[IV]}Fe^{3+}$, $^{[V]}Fe^{3+}$), so acting both as a network former and a network modifier. This because aluminium and iron exceed the amount that can be incorporated in the tetrahedral network by charge compensation. As a consequence, Fe^{2+} will be promoted, as it will be able to participate in charge compensating Al-bearing polyhedral units [30,36,56]. It is therefore expected that Fe^{3+} will occupy a stable position in peralkaline melts, while it will be suppressed in peraluminous melts, leading to lower Fe^{3+}/Fe_{tot} ratios (Figure S1, supplementary material). Considering the quite large compositional perimeter of porcelain stoneware [14,23] where Na is the dominant network glass modifier, the influence of K, Ca, Mg [30,35,49,57] and silica content [58] must also be taken into account.

The presence of iron with different valence states and structural roles, which tend to change according to temperature and melt composition, has important effects on the key properties for the sintering process (primarily the viscosity of the liquid phase). Furthermore, it may be important for the densification efficiency, because of the possible oxygen release during the passage from an oxidized to a reduced atmosphere – linked to the $Fe_2O_3^{melt} = 2\ FeO^{melt} + \frac{1}{2}O_2^{gas}$ equilibrium [26,30] – that can boost bloating phenomena [59].

The variation of the Fe^{3+}/Fe_{tot} ratio, in particular, may involve a significant change in the melt viscosity for silica-rich compositions [30,44–46,51], while it has substantially negligible change for the viscosity of depolymerized melts at high temperature and variations up to about 1 log units at close to glass transition (e.g. [48,52]). In fact, as long as trivalent iron is a glass network former, then charge compensated mostly by alkalis, the viscosity decrease is modest with respect to an analogous melt containing Al [30]. Indeed, comparing the viscosity at 1400 °C along the meta-aluminous SiO_2-$NaAlO_2$ and meta-ferric SiO_2-$NaFeO_2$ joins, the drop is within 0.2 log_{10} Pa·s [45]. Coordination changes of Fe^{3+} – expectable for peraluminous melts – are thought to induce extremely small variations of viscosity [30]. A decrease of the Fe^{3+}/Fe_{tot} ratio, however, has a more accentuated effect: for instance, lowering this ratio from 0.9 to 0.5 in the $NaFeSi_2O_6$ system brings a drop of around 0.35 log_{10} Pa·s at 1430 °C as a consequence of more Fe^{2+} as glass network modifier [44].

3. Experimental

3.1. Materials

Five different batches were designed by using red clays to reach sufficiently high iron contents to attain the detection limit of Mössbauer spectroscopy. Ceramic samples were obtained and characterized in a previous study, which aimed to assess the feasibility of incorporating high amounts of iron into porcelain stoneware [20]. The formulations considered are: a benchmark, named B0, representing a classical industrial formulation for porcelain stoneware, and four batches containing, among other ingredients, 20 wt% or 35 wt% of a German red clay (GBC20 and GBC35, respectively) and 10 wt% or 20 wt% of an Italian red clay (MMP10 and MMP20, respectively). Batch formulations are reported in Table S1 (supplementary material).

These batches underwent the simulation of the industrial tile-making process at the laboratory scale. The tiles were fired at different maximum temperature (T_{max}) based on their thermal behaviour: B0, GBC20, GBC35 at T_{max} = 1160, 1180, 1200, 1220 and 1240 °C, while MMP10 and MMP20 at T_{max} = 1140, 1160, 1180, 1200 e 1220 °C. Details on the mineralogical characterization of raw materials and technological behaviour of bodies can be found in Fantini et al. [20].

3.2. Methods

The chemical analysis of the batches was carried out by wavelength-dispersive X-ray fluorescence spectrometry by a Zetium Panalytical instrument and by applying the methods proposed by Franzini et al. and Leoni and Saitta [60,61]. Measurements were performed on pressed powder pellets. Analyses are considered accurate within 2–5 wt% (relative) and the precision is estimated on the second decimal place. Results are reported in Table 1.

The quantitative phase analyses of both raw batches (Table 1) and fired tiles (Table S2, supplementary materials) were performed by Rietveld refinement. X-Ray powder diffraction patterns were collected using a θ–θ Bragg-Brentano PANalytical 'XPert Pro Diffractometer equipped with a Cu Kα radiation (λ 1.5418 Å) tube operating at 40 kV and 40 mA and with a real time multiple strip (RTMS) detector. Samples were ground using an agate mortar and the powder was mixed with 10 wt% of corundum (α-Al_2O_3) NIST 676a as an internal standard. Data were collected in the angular range 3–110°2θ using step scan of 0.0167°2θ and a counting rate of 12 s/step. A 0.5° divergence slit was used and 0.04° Soller slits. The XRPD patterns were analyzed using the X-Pert High Score Plus suite. To obtain quantitative phase analyses the Rietveld method [62] was exploited, and the data were fitted using the the Profex version 5.2.9 software [63] for the raw batches and the EXPGUI interface [64] GSAS package [65] for the fired tiles. Details of refinements are reported in Table S2, while selected XRPD patterns are shown in Figure S2 (both in supplementary materials).

The quantitative chemical and phase compositions of every fired body were used to calculate the chemical composition of the amorphous phase by subtracting the contribution of each crystalline phase, considering its stoichiometric formula, from the bulk chemistry. The values so obtained were normalized to 100 wt% (Table S3, supplementary materials). For details on data interpretation and calculation of parameters about chemical composition and pseudostructural parameters of the melt, see relevant literature [21,24,30,54,66,67]. Remarks about the representation of the chemical composition of amorphous phases at different temperatures in the SiO_2–Al_2O_3–Na_2O_{eq} ternary diagram are given in Conte et al. [67]. The physical properties of the non-crystalline phase at high temperature were estimated by predictive models based on its chemical composition. The shear viscosity was calculated based on the Giordano and co-workers' model [68], and the gas–liquid surface tension was estimated interpolating the data obtained

Table 1

Chemical and mineralogical composition of clays and porcelain stoneware bodies.

Component	unit	Clay raw materials		Porcelain stoneware bodies				
		GBC[a]	MMP[a]	B0	GBC20	GBC35	MMP10	MMP20
SiO_2	wt%	62.22	53.81	68.75	70.74	72.29	68.56	67.87
TiO_2	wt%	1.16	0.74	0.69	0.70	0.71	0.63	0.58
Al_2O_3	wt%	18.43	16.82	19.73	17.93	16.61	18.54	17.91
$Fe_2O_{3\ total}$	wt%	2.66	7.1	0.60	1.08	1.43	1.16	1.72
MgO	wt%	0.6	3.28	0.48	0.44	0.40	0.7	0.98
MnO	wt%	0.01	0.18	0.01	0.01	0.01	0.02	0.04
CaO	wt%	0.13	1.43	0.61	0.51	0.47	0.66	0.79
Na_2O	wt%	0.16	1.56	3.70	3.75	3.7	3.98	4.08
K_2O	wt%	1.81	2.97	1.42	1.39	1.36	1.55	1.68
P_2O_5	wt%	0.05	0.11	0.3	0.26	0.25	0.36	0.37
LOI	wt%	12.76	12	3.56	3.04	2.62	3.69	3.81
Alumina saturation index[b]	1	-	-	1.98	1.85	1.76	1.66	1.44
Alumosity[c]	mol.	-	-	76.9	75.3	74.3	73.2	70.3
Hematite	wt%	1.0(1)	0.6(1)	n.d	0.3(1)	0.3(1)	0.1(1)	0.3(1)
Kaolinite	wt%	19.0(3)	10.7(4)	11.4(5)	12.2(8)	15.6(9)	11.1(6)	12.3(6)
Illite/mica	wt%	10.5(2)	17.1(7)	10.9(3)	10.8(5)	9.6(4)	11.2(3)	11.3(5)
I/S Mixed Layers	wt%	12.7(4)	34.0(7)	6.6(6)	2.6(7)	4.4(5)	3.5(7)	6.7(6)
Quartz	wt%	44.5(2)	18.3(2)	30.2(3)	35.1(4)	34.2(4)	31.2(3)	27.9(3)
Plagioclase	wt%	3.8(2)	7.9(2)	40.5(3)	38.4(4)	35.3(4)	41.0(4)	39.6(4)
K-feldspar	wt%	6.7(3)	7.5(3)	n.d.	0.2(2)	n.d.	1.2(3)	0.7(3)
Calcite	wt%	0.3(1)	1.7(1)	n.d.	n.d.	n.d.	0.2(1)	0.5(2)
Accessories[d]	wt%	1.4(2)	2.2(2)	0.4(2)	0.4(2)	0.6(2)	0.5(2)	0.7(2)

[a] data from Fantini et al. 2024;

[b] the alumina saturation index represents the amount of Al_2O_3 not provided by feldspars;

[c] the alumosity is a chemical parameter defining the ratio between $Al_2O_{3eq}/(Al_2O_{3eq} + Na_2O_{eq})$, where Al_2O_{3eq} represents the sum of Al_2O_3 plus Fe_2O_3 (expressed as molar equivalent of Al_2O_3) while Na_2O_{eq} represents the sum of Na_2O plus K_2O, MgO and CaO (expressed as molar equivalent of Na_2O)

[d] accessory phases are: rutile for GBC; chlorite, dolomite, anatase and rutile for MMP; rutile and anatase for all the porcelain stoneware bodies.

by Appen's and Dietzel's methods [69,70]. The melt timescale was calculated based on Vasseur et al. [71]. Moreover, the effective viscosity of the body (η_{eff}) was calculated as the product of the shear viscosity of the melt (η_{melt}) by the relative viscosity (η_{rel}), i.e., $\eta_{eff} = \eta_{rel} \cdot \eta_{melt}$ [21,67]. The relative viscosity was estimated by the relation: $\eta rel = [1-(\phi/\phi_m)]^{-B\phi m}$, where ϕ is the solid load, ϕ_m is the critical fraction and B is the Einstein constant (i.e., $B = 2.5$) [72]. Results reported in Table S3.

Room temperature Mössbauer spectroscopy experiments were performed at Department of Chemical Science, University of Padua, using a constant acceleration spectrometer mounting a room-temperature Rh matrix ^{57}Co source, nominal strength 1850 MBq. Only samples with the highest percentage of iron were analyzed, i.e., bodies GBC35 and MMP20 as well as the raw clays GBC and MMP. The spectra of raw materials were collected by placing $\approx$80 mg of grinded powder dispersed in petrol jelly in a 17 mm diameter sample holder. Due to the dilution of the raw material, the spectra of the porcelain body formulation, unfired and fired, were collected on $\approx$1000 mg of material, mixed with petroleum jelly, placed in a 38 mm sample holder. Depending on the sample, a LND, INC cylindrical proportional 4011 or 4012 mm was used. The obtained spectra were fitted to Lorentzian line shapes using a minimum number of sextets and doublets. The obtained hyperfine parameters, isomer shift (δ), quadrupole splitting (Δ) or quadrupole shift (ε) when magnetic coupling is present, half linewidth at half maximum (Γ_+), are expressed in mm/s, while the internal magnetic field (B) in Tesla and the relative areas (A) in %. The velocity was calibrated against a α-Fe foil and δ is quoted relative to metallic iron at room temperature. Recoilless fractions f for Fe^{2+} and Fe^{3+} were considered equal [73]. Given the significant error inherent in the area evaluation, this approximation is acceptable. The instrumental error is presumed to be greater than the error incurred by evaluating the areas without considering different f values. Every attempt to fit the paramagnetic components in the spectra of the fired materials using a Gaussian distribution for the quadrupole splitting (QSD model according to Voight-based methods [74]) failed to yield satisfactory results.

The sintering behavior of all the ceramic bodies was evaluated by hot stage microscopy, using an optical thermo-dilatometer (TA, ODP868, Germany) which registered the size variation of a 5 ×5×5 mm chip cut from the dry samples, determined by the pixel count during a thermal cycle. The tests were run under isothermal conditions at different maximum temperatures corresponding to the firing ones, with a gradient of 80 °C/min^{-1} and dwell time of 30 min. Different stages of the sintering process were identified with reference to Figure S3 in Conte et al. [24]. Isothermal sintering rates were calculated for linear shrinkage (neck formation stage), decreasing shrinkage (vented bubble stage), total sintering and bloating, deriving from specimen height variation by dwell time at the various maximum temperatures. Results reported in Table S4.

The microstructural evolution of the fired ceramic batches was studied by a scanning electron microscope (JSM-6010 LA InTouchScope, graphite sputtered polished surface, JEOL, USA), and images were collected using backscattered electrons.

4. Results and discussion

4.1. Composition of porcelain stoneware bodies

The chemical and mineralogical composition of the bodies is summarized in Table 1, which also reports data of the red clays used (GBC and MMP).

In the batch formulation, a replacement of conventional ball clay with red clay was performed, without changing the clay/flux/filler ratios to ensure proper workability of the body. Although the content of feldspars was substantially constant, variations occurred in the percentage of quartz (higher in GBC20-GBC35 bodies) and in the clay minerals assemblage (kaolinite-illite-I/S mixed layers). This has unavoidably changed the ratio between alumina (or $Al_2O_3+Fe_2O_3$) and alkaline and alkaline-earth oxides, as evidenced by alumina saturation index (ASI), that is decreasing from the benchmark B0 to the body MMP20 (Table 1). Iron was present in raw materials essentially as hematite (especially in GBC), and in the phyllosilicates structure (illite, kaolinite, and mixed-layers). The levels of amorphous phase in the samples are below the detection limits, so if Fe-oxyhydroxides with a

low structural order are present, could be only in very small percentages. This is consistent with the in-depth characterization of the clay reported by Fantini et al. [20]. The mineralogical composition of the batches matches the mineralogical analyses of the clays used and their percentages in calculations. Probably, the amount of hematite is slightly overestimated in the MMP samples, but considering the low percentage and the errors, the results are consistent with raw materials mineralogical composition.

4.2. Iron speciation in raw materials

Mössbauer spectroscopy, probing the local interactions at the Fe nuclei, describes the distribution of Fe over the mineralogical assemblage in the two raw materials (GBC, MMP). The spectrum collected on the red clay GBC (Fig. 1a) clearly shows the presence of two distinct components: an intense sextet, due to the presence of magnetically coupled Fe, together with a weak and not well resolved doublet, ascribed to Fe in the silicate structures.

The sextet exhibits hyperfine parameters, reported in Table 2, clearly attributable to Fe^{3+} occupying the hematite octahedral site, while the doublet can be related to the distorted octahedral Fe^{3+} in the layered silicates. It is interesting to observe that the B value is slightly lower than the theoretical one (50.9 T instead of 51.7 T) as a possible consequence of Fe^{3+} substitution by Al^{3+} [75].

Concerning the Fe^{3+} in layered silicates, the quite large linewidth suggests the superimposition of contributions from various sites, each differing for the Δ value. Such Fe^{3+} distorted octahedral sites are likely in kaolinite and/or illite octahedral sites. Unlike GBC, the clay MMP does not exhibit the intense sextet due to the presence of Fe oxides. The spectrum collected in the ± 10 mm/s range shows the presence of an intense and complex paramagnetic absorption together with a weak sextet. The intensity of the sextet, obtained by a preliminary fit, is less than 10 % of the total Fe. Due to the extremely low intensity, the hyperfine parameters are affected by notable uncertainty, therefore this signal can be only related to a generic Fe^{3+} oxide. This is consistent with the low amount of hematite found in the raw clay. To enhance the distribution of Fe in the paramagnetic absorption, the measurement was performed in the ± 4 mm/s range for the MMP clay (Fig. 1b). The best fitting reveals contributions from three different sites: two ascribed to Fe^{3+} and one to Fe^{2+}. The two Fe^{3+} sites are representative of octahedral sites differing each other for distortion: the former exhibiting the lowest Δ value is representative of highly symmetric sites, while the latter can be associated with distorted octahedral sites (Table 2). Concerning the third doublet, it has the typical hyperfine parameters of distorted octahedral sites. In both samples, the hyperfine parameters associated with

Table 2

Hyperfine parameters obtained from the Room Temperature Mössbauer spectra collected on the raw clays. The sum of the relative areas in MMP is less than 100 % due to the presence of not properly fittable tiny amount of Fe^{3+} oxide. δ is quoted relative to α-Fe foil. M: octahedral sites.

Sample	δ (mm/s)	Δ (mm/s)	Γ_+ (mm/s)	B (T)	A (%)	Attribution
GBC	0.31 ± 0.05	0.55 ± 0.09	0.22 ± 0.09		32 ± 2	Fe^{3+} M
	0.38 ± 0.03	-0.14 ± 0.03	0.19 ± 0.05	50.7 ± 0.2	68 ± 5	Fe^{3+} M in α-Fe_2O_3
MMP	0.36 ± 0.07	0.50 ± 0.03	0.23 ± 0.08		47 ± 3	Fe^{3+} M
	0.34 ± 0.09	0.87 ± 0.01	0.29 ± 0.01		15 ± 1	Fe^{3+} M
	1.09 ± 0.02	2.57 ± 0.03	0.19 ± 0.04		31 ± 2	Fe^{2+} M

the paramagnetic sites indicate the presence of Fe species in clay minerals, specifically Fe^{3+} can be hosted at the octahedral site either of kaolinite or illite, while Fe^{2+} can be preferentially hosted at the illite octahedral site. According to literature [76–78], Fe^{3+} in the octahedral sites of kaolinite, illite, and smectite typically shows δ values ranging from 0.29 to 0.38 mm/s and Δ between 0.50 and 1.0 mm/s. On the other hand, Fe^{2+} in octahedral environment is usually associated with the presence of micas, and sometimes in kaolinite, and it is characterized by δ values close to 1.00–1.30 mm/s and Δ higher than 2.0 mm/s [79–81].

The formulation of the porcelain stoneware bodies results, considering the Fe point of view, in a dilution of sample. The spectra of these materials, reported in Figure S3, are clearly similar those of collected in raw materials with a considerable decrease in the Mössbauer effect. The obtained hyperfine parameters are consistent with those obtained on the raw materials and are reported in Table S5. It is interesting to note that the tiny sextet in MMP spectrum completely disappears in the spectrum collected on the formulation MMP20.

4.3. Phase transformations during firing

The technological study of the porcelain stoneware bodies revealed that "*the substitution of classic ball clays with red clays did not introduce unsolvable bottlenecks in ceramic tile production*" [20]. In that paper, the mineralogical study focused on the temperature of maximum densification only, while in the present work phase transformations are followed during the whole sintering process and even in overfiring conditions. All data are summarized in Table S2 (supplementary material) and the trends of major phases as a function of firing temperature
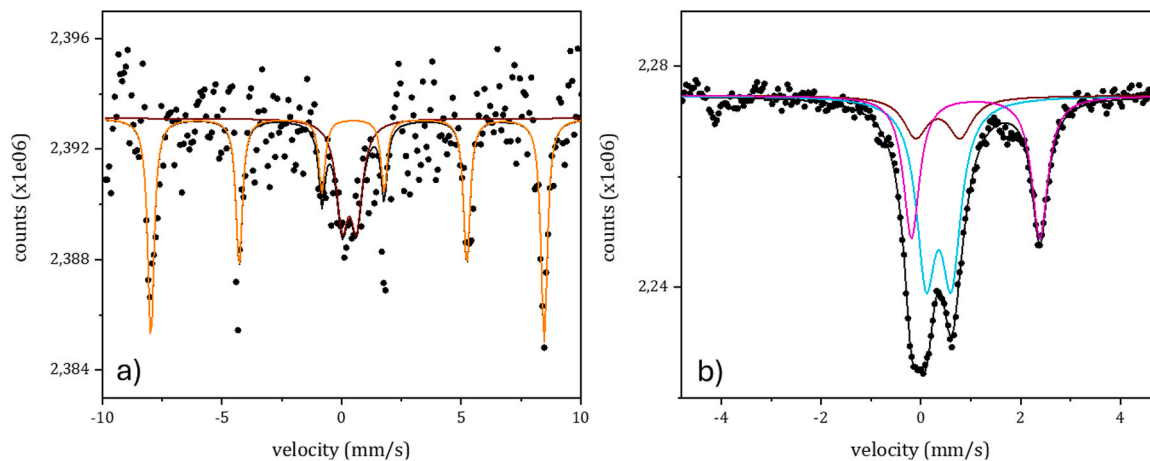

Fig. 1. Room Temperature Mössbauer spectra collected on: GBC clay (a) and MMP clay (b). Black dots are the experimental data; black lines represent the calculated spectra, wine and cyan lines represent the subspectra relative to paramagnetic Fe^{3+} in phyllosilicates, while the magenta line is relative to paramagnetic Fe^{2+} in the same mineralogical assemblage. The orange lines in a) are related to the subspectrum of to Fe^{3+} in hematite.

are drawn in Fig. 2.

Quartz exhibits a moderate but non-negligible decrease (<25 wt% of the original content) as the temperature increased for all bodies, confirming previous studies on porcelain stoneware [21,22,82]. These variations have roughly the same slope as in the benchmark (B0), thus indicating that the reactivity of quartz during firing did not vary substantially in the presence of red clay. The difference in the absolute contents after firing reflects the starting compositions: the GBC20-GBC35 batches contain more quartz than B0, due to the addition of the German red clay that is richer in quartz.

Plagioclase melted more or less at the same rate in all batches. In contrast, K-feldspar was not detected in any of the bodies, indicating that it completely disappeared already at 1140 °C, as usually observed in sodic porcelain stoneware [21,83]. However, the percentage of plagioclase in the bodies at maximum densification was variable due to the different temperatures needed for gresification (1200 °C for B0, 1220 °C for GBC20 and GBC35, 1180 °C for MMP10 and 1160 °C for MMP20). The residual amount of plagioclase was lower than the benchmark for GBC20-GBC35 batches, but significantly higher for MMP10-MMP20 (Fig. 2 and Table S2). This appears to be coherent with the different firing temperatures.

Mullite persisted as the temperature rose, substantially in line with the literature [84,85], with slight fluctuations, more marked for MMP samples, due to crystallisation and dissolution reaction occurring at the different temperatures. All iron-rich formulations contain less mullite than the benchmark, particularly MMP20. The absolute amount of mullite seems not only linked to the initial kaolinite contents but also to the alumina saturation degree (Table 1).

The amorphous phase grew almost constantly as the temperature increased, and at about the same rate in all formulations, always falling within the typical range of porcelain stoneware [21,23]. The degree of vitrification at the different temperatures of maximum densification (T_{md}) was slightly higher than the benchmark for GBC20, equivalent for GBC35 and lower for the MMP batches.

The effect of different red clays on the firing behaviour of porcelain stoneware seems mainly related to the overall composition of the batches (Table 1). In particular, the higher quartz content of the GBC clay or the higher contents of I/S mixed layers and feldspars of the MMP clay affect more than the increased amount of iron.

Most of iron is incorporated in the vitreous phase, where the $Fe_2O_{3\ tot}$ percentage decreased with firing temperature, due to dilution by gradual melting of feldspars. At the temperature of maximum densification, $Fe_2O_{3\ tot}$ attained ~1 wt% in the benchmark, 1.5 wt% in GBC20, 1.9 wt% in GBC35 and in MMP10, and 3 wt% in MMP20 (Fig. 3A). Hematite was detected only in the bodies with Fe-rich clays, even though in very small amounts: around 0.3 wt% in GBC35 and in the 0.1–0.2 wt% range in the others (Fig. 3B).

The phase evolution of the investigated bodies results in diversified vitrification paths (that is, the amount and composition of the liquid phase as the temperature increases). The composition of the amorphous phase at the lowest temperature considered here is highly peraluminous as it results from the breakdown of clay minerals and K-feldspar and a limited melting of plagioclase. Paths move, as the temperature increases, towards less peraluminous and more siliceous compositions, depending on the progressive fusion of plagioclase and quartz (Fig. 4). The paths followed by the B0 and the GBC20-GBC35 bodies are very close, differing from those of MMP10 and especially of MMP20, mainly due to the content of silica, at similar alumosity values (Fig. 4).

4.4. Iron speciation in porcelain stoneware

In general, the firing (including overfiring) of the ceramic bodies had two main effects on the Fe speciation: a re-distribution of the Fe moieties among crystalline (e.g. [86]) and amorphous phases together with a shift in the $Fe^{3+} \rightleftarrows Fe^{2+}$ equilibrium. The re-distribution of the Fe-species is particularly evident in GBC35. In comparison with the unfired material, the spectrum collected after firing at 1220 °C shows a clear decrease in intensity of the magnetic pattern together with the broadening of the central paramagnetic absorption (Fig. 5a). The best fitting concerns a four components model: two sextets, ascribed to Fe^{3+} oxides, and two doublets, assigned to Fe^{3+} and Fe^{2+}, respectively. Both sextets exhibit hyperfine parameters (Table 3) assigned to Fe^{3+} in distorted octahedral sites. The former, distinguishable for the highest B value, is representative of Fe^{3+} hosted in the hematite lattice. Considering all the hyperfine parameters, it is reasonable to suppose that this signal is relative to hematite originally present in the GBC clay. The latter sextet could be related to a new disordered ferric oxide, presumably nucleated in the amorphous matrix of the ceramic batch. Its hyperfine parameters are compatible with those of a highly substituted hematite. Indeed, the low B value reflects the fact that Al^{3+} ions replace Fe^{3+} ions in hematite particles [75].

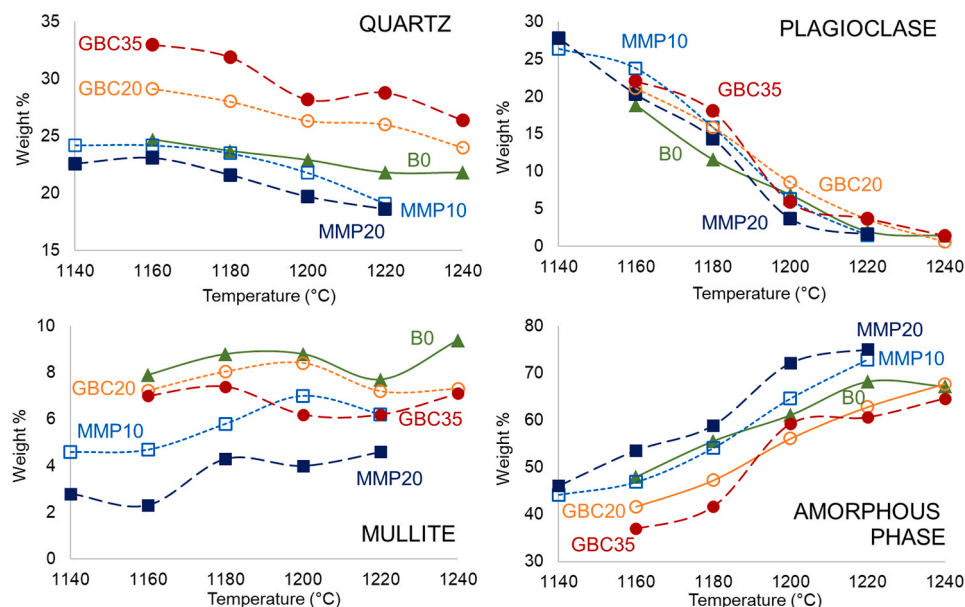The quadrupole shift value (ε) close to zero, certainly smaller

Fig. 2. Phase composition (% weight) of porcelain stoneware bodies as a function of firing temperature (°C). Experimental error is within the symbol size.
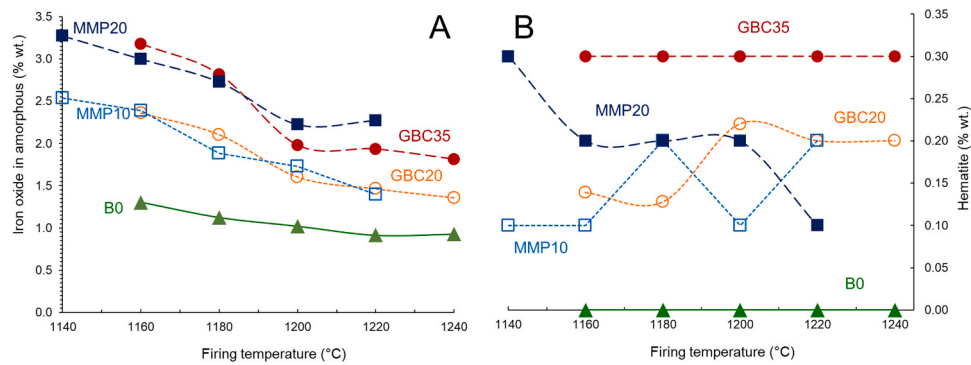
Fig. 3. Iron partition in porcelain stoneware bodies: Fe_2O_3 total in the amorphous phase (A) and hematite (B) as a function of firing temperature. Experimental error is within the symbol size.
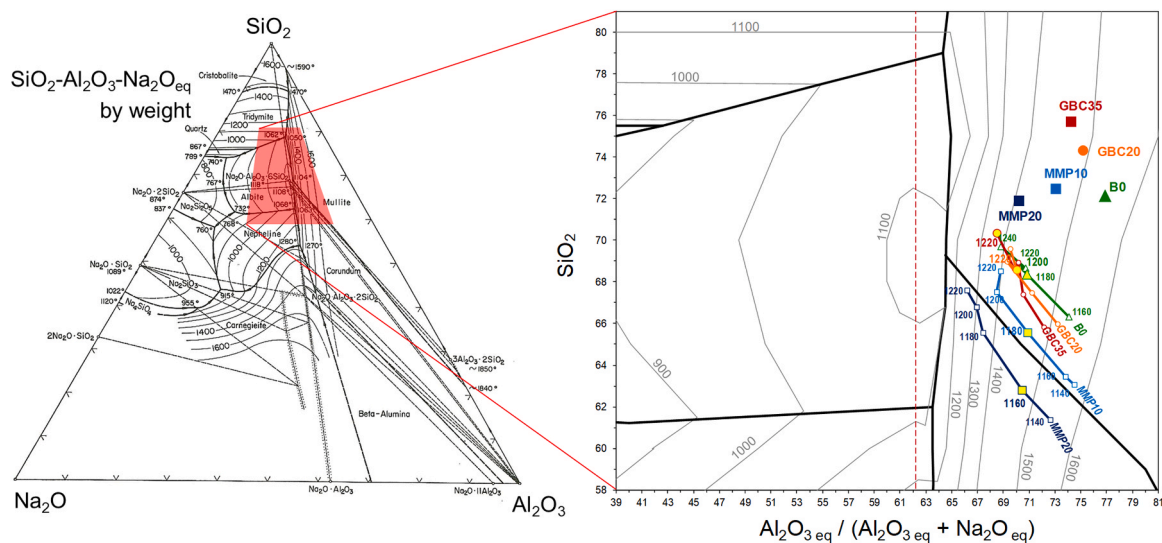

Fig. 4. Alumosity-silica diagram with batch compositions (full symbols) and vitrification paths (melt composition at different temperatures) with maximum densification highlighted. For the diagram construction, see Conte et al. [67].

compared to −0.197 mm/s for well-crystallized hematite, suggests an antiferromagnetic behavior [87]. This evidence could be related to the presence of small, highly substituted hematite particles, nucleated and grown in the amorphous phase of the ceramic batch. Considering the intensity of the magnetic pattern, the firing halved the total amount of ferric oxide originally present in the unfired material. According to other experimental data, the firing promoted the dissolution of hematite with incorporation of Fe^{3+} in the melt and, at the same time, the shifting of the $Fe^{3+} \rightleftarrows Fe^{2+}$ equilibrium towards the reduced species. The central paramagnetic absorption shows a clear shoulder at high velocity values, suggesting the presence of ferrous moieties. As mentioned before, the paramagnetic components were fitted by two doublets: one attributed to six-fold Fe^{3+} ions, the other representative of Fe^{2+} ions. The ferric site is considerably different from the sites occurring in the starting raw material: the large Δ suggests a remarkable distortion of the site geometry and the broad linewidth reflects that ions are hosted in an amorphous matrix. The linewidth broadening is, as matter of fact, congruent with the existence of various Fe^{3+} sites, slightly different from each other, due to distortion of the coordination octahedron or substitution in the second coordination sphere, as in a vitreous matrix. Nevertheless, the presence of Fe^{3+} sites attributable to crystalline phases, such as mullite [88], superimposed to those belonging to the vitreous matrix, cannot be excluded a priori. While in ferric sites δ can readily serve as an indicator of the oxygen coordination number, defining the site geometry for the newly formed ferrous sites within the amorphous matrix by using δ is

more complex. Literature data on Na, K, Ca or Mg silicate glasses [36,89, 90] suggest that a δ between 0.8 mm/s and 1.15 mm/s can be representative of a range of coordination states. These approach a 4-fold coordination, when δ is close to the lowest value, while 5- or 6-fold when δ is close to the highest value. According with these interpretations, we can reasonably assume that the obtained δ can be representative of Fe^{2+} in five-fold coordination and or six-fold coordination geometry [36] even though the occurrence of nanophasic magnetite nuclei cannot be excluded [91].

The overfiring at 1240 °C (Fig. 5b) especially affected the $Fe^{3+} \rightleftarrows Fe^{2+}$ equilibrium. The Mössbauer spectrum is close to that at T_{md}, and can be fitted using the same four components model. As matter of fact, the amount of Fe^{2+} increases to 20 % and the broad linewidth supports that this site is in the vitreous matrix. It is worthy to note that the increasing in ferrous component took place at the expense of the ferric ions in the glass rather than those hosted in the hematite lattice. The overall intensity of the Fe^{3+} oxides did not essentially change after overfiring, while the intensity of the ferric doublet decreased. Concerning the sites geometry of the paramagnetic Fe^{3+} and Fe^{2+}, no drastic variation were observed. The iron speciation in GBC35 is reported in Fig. 6. The firing of MMP20 promoted a partial oxidation of the ferric ions hosted in the clay minerals, together with the increase of the magnetically coupled species. The spectrum at the T_{md} (1160 °C) was fitted by a three components model (Fig. 5c): two doublets, ascribable to ferric and ferrous species, and a sextet. The latter exhibits hyperfine parameters (Table 3) typical of
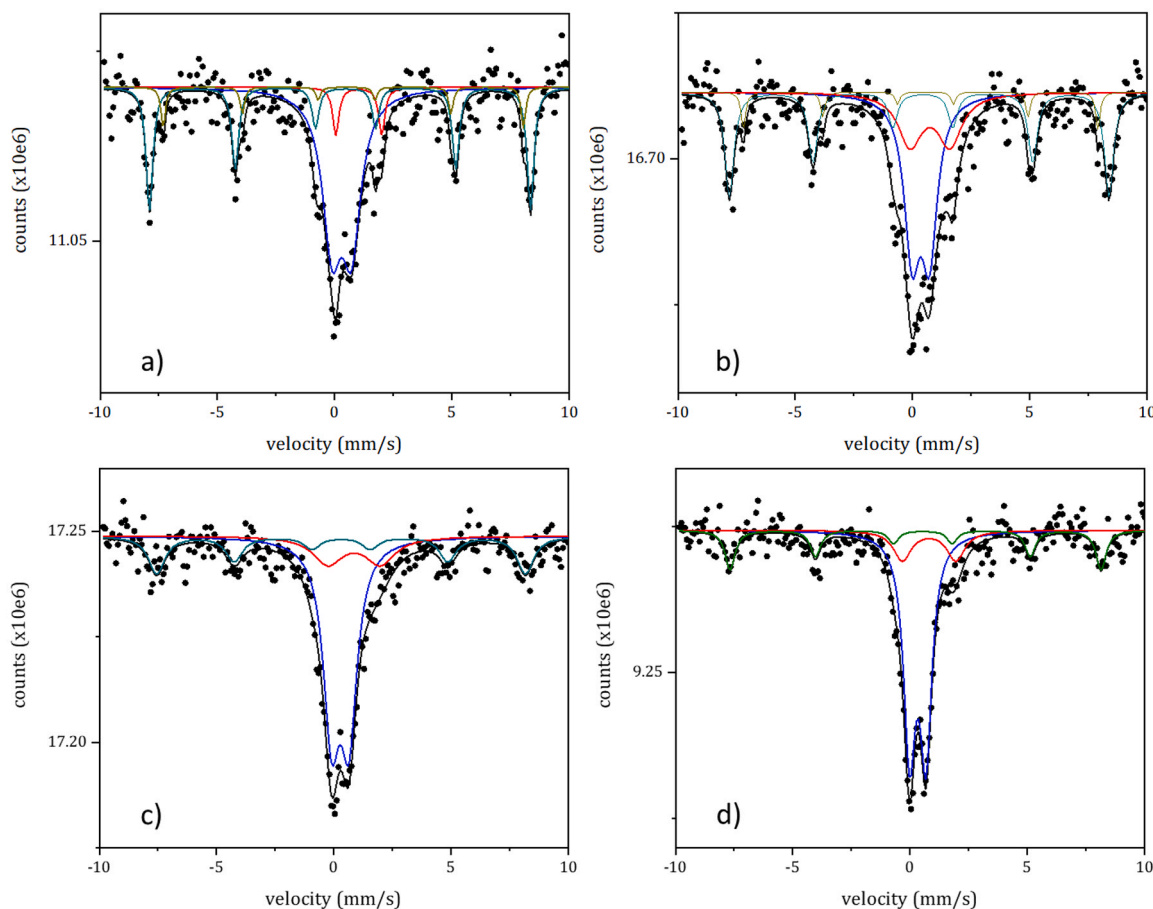
Fig. 5. Room Temperature Mössbauer spectra of: GBC35 fired at 1220 °C (a) and at 1240 °C (b); MMP20 fired at 1160 °C (c) and at 1200 °C (d). Black dots experimental data, black lines represent the calculated spectra, blue lines the subspectra relative to paramagnetic Fe^{3+}, red lines the subspectra relative to paramagnetic Fe^{2+} while the green lines the subspectra relating to Fe^{3+} in hematite. The ochre lines in a) and b) are related to the subspectra of the oxide phase containing newly formed Fe^{3+}.

octahedrally-coordinated Fe^{3+} ions in Al-substituted hematite, and it represents 20 % of the total Fe. The two doublets have parameters characteristic of six-fold ferric and ferrous ions, respectively. These components differ substantially from those observed in the raw materials; considering the hyperfine parameters, it is evident that these sites belong to the amorphous matrix: the large Δ and the broad linewidth are typical of Fe hosted in glassy phases. Contrary to GBC35, the overfiring of MMP20 at 1200 °C (Fig. 5d) did not promote any substantial variation of the spectrum with respect to T_{md}.

The speciation of Fe seems to be at equilibrium (Fig. 6), which corresponds rather well to the Fe^{3+}/Fe_{tot} ratio predicted by the chemical composition of the vitreous phase at the firing conditions [54]. Even though the overfiring did not affect the $Fe^{3+} \rightleftarrows Fe^{2+}$ equilibrium, the ferric site geometry seems to be influenced by the increasing in firing temperature. As matter of fact, the overfiring promotes a decrease in δ, from 0.33 to 0.27 mm/s, indicating the presence of Fe^{3+} in tetrahedral sites. The stabilization of 4-fold Fe^{3+} can be ascribed to the local charge balance by the M^+ and M^{++} cations contained in the melt [92,93]. However, given the low resolution of the spectrum, which is a result of the minimal Fe content, it cannot be definitively ruled out that a doublet due to octahedral Fe^{3+} might be superimposed on the one corresponding to tetrahedral Fe^{3+}. Every attempt to fit the spectrum with two Fe^{3+} different doublets did not bring satisfactory results; it was therefore preferred to use a single ferric doublet model.

4.5. Composition and physical properties of the vitreous phase

The chemical composition and physical properties of the vitreous phase at all firing temperatures are reported in Table S3 (supplementary material) while data for samples fired at the temperature of maximum densification and two overfiring (GBC35 at 1240 °C and MMP20 at 1200 °C) are summarized in Table 4.

Changes in the overall composition of the vitreous phase can be better followed as a function of glass depolymerization (NBO/T) and pseudostructural parameters (Fig. 7). The variations in the iron content of the melts (Fig. 3A) have been already discussed in the previous sections.

All bodies show an increasing in glass polymerization, denoted by lowering of the calculated NBO/T, as a function of the dissolution of mineral phases with increasing firing temperature (Fig. 7A). This is due both to the increase of silica content, mainly by quartz and plagioclase melting. Both phenomena favoured a growth of glass network formers with temperature increasing. The trend is not linear, as it reflects the greater fusion of plagioclase and quartz in the 1160–1200 °C range (Fig. 7B). On the other hand, the content of glass network modifiers is perfectly related to the value of NBO/T (Fig. 7C). The charge compensation mechanism, which allows the incorporation in tetrahedral coordination of Al^{3+} and Fe^{3+} in substitution of Si^{4+}, occurs in complex way, as soon as the peraluminous boundary is overcome. In fact, the dissolution of Fe^{3+} may be suppressed in favour of Fe^{2+}, and both ferric and ferrous cations can play the network modifier role. In addition, Fe^{2+} might even act as network compensating cations too. This makes it

Table 3
Hyperfine parameters obtained from the Room Temperature Mössbauer spectra collected on the fired porcelain stoneware bodies; δ is quoted relative to α-Fe foil. M: octahedral sites, T: tetrahedral sites, P: pentacoordinate.

Sample	Firing T (°C)	δ (mm/s)	Δ (mm/s)	Γ_+ (mm/s)	B (T)	A (%)	Attribution
GBC35	1220	0.30 ± 0.06	0.8 ± 0.1	0.4 ± 0.1		54 ± 4	Fe^{3+} M
		1.03 ± 0.09	1.9 ± 0.2	0.2 ± 0.1		6 ± 1	Fe^{2+}
		0.34 ± 0.03	−0.12 ± 0.03	0.17 ± 0.05	50.4 ± 0.2	33 ± 2	Fe^{3+} M in α-Fe_2O_3
		0.43 ± 0.07	−0.07 ± 0.07	0.11 ± 0.09	47.6 ± 0.5	7 ± 1	Fe^{3+} M in Fe^{2+} ox
	1240	0.36 ± 0.07	0.8 ± 0.1	0.4 ± 0.1		46 ± 3	Fe^{3+} M
		0.94 ± 0.09	1.83 ± 0.06	0.6 ± 0.1		15 ± 1	Fe^{2+}
		0.36 ± 0.04	0.07 ± 0.04	0.23 ± 0.06	50.2 ± 0.4	32 ± 2	Fe^{3+} M in α-Fe_2O_3
		0.45 ± 0.09	−0.10 ± 0.09	0.11 ± 0.08	46.9 ± 0.9	6 ± 1	Fe^{3+} M in Fe^{2+} ox
MMP20	1160	0.33 ± 0.02	0.69 ± 0.04	0.30 ± 0.04		66 ± 4	Fe^{3+} M
		0.8 ± 0.2	2.3 ± 0.1	0.46 ± 0.09		14 ± 1	Fe^{2+}
		0.39 ± 0.08	−0.16 ± 0.08	0.25 ± 0.09	49.0 ± 0.6	20 ± 1	Fe^{3+} M in α-Fe_2O_3
	1200	0.27 ± 0.03	0.73 ± 0.08	0.42 ± 0.08		60 ± 4	Fe^{3+} M
		0.8 ± 0.1	2.2 ± 0.1	0.7 ± 0.1		16 ± 1	Fe^{2+}
		0.39 ± 0.09	0.02 ± 0.09	0.42 ± 0.09	48.7 ± 0.9	24 ± 2	Fe^{3+} M in α-Fe_2O_3

difficult to exactly predict amount of charge compensators and put it in relationship with the melt polymerization (Fig. 7D). As a matter of fact, the content of alkali and alkali-earths in the melt is almost constant with the temperature (Table S3, supplementary material). Such a content is entirely used for charge compensation already since 1140–1160 °C, so that glass network modifiers are basically made up of Al and Fe in these liquid phases that are clearly peraluminous (Fig. 4). As the firing temperature increased, the liquid phase composition was changed by progressive melting of quartz and feldspars, leading to a clear decrease in glass network modifiers.

The variations in the compositional characteristics of the liquid phase affected the physical properties: a decrease in both shear viscosity and the surface tension of the melt was observed as the temperature increased (Fig. 8). Trends are not always regular, as they reflect the above-mentioned variations of phase composition.

The viscosity of silica- and alumina-rich, iron-enriched melts is lower than that of the benchmark. This difference is small for bodies GBC20-GBC35 and more accentuated for MMP10 and particularly MMP20. This likely reflects the relatively lower silica content and the differences in both the content and the speciation of iron for the investigated peraluminous residual melts. They will require both the experimental rheological analysis of the residual liquid product associated to a structural spectroscopic analysis of these complex systems at both high temperature and low temperature at close to the glass transition [42,68].

The estimated surface tension varies over a narrow range and the values for MMP10 and GBC20 are very close to those of the B0. The bodies with the greatest iron content exhibit a contrasting behaviour, with the highest (MMP20) and the lowest (GBC35) surface tension values. This is marginally influenced by iron and more by silica, alumina and fluxing oxides.

The timescale can be taken to jointly assess the effects of viscosity and surface tension. It shows that the reaction times of MMP10-MMP20 bodies are significantly faster than those of the benchmark and GBC20-GBC35 bodies, which are similar above 1190 °C. This is a reflection of the enrichment of Fe, Ca and Mg and the decrease in silica, which dictate a decrease in viscosity and a simultaneous increase in surface tension of the melts (MMP). In parallel, iron and silica enrichment is less influential (GBC).

Moreover, the effective viscosity (i.e., the viscosity of the bulk: liquid plus solid phases) presents a dichotomy between benchmark and GBC20-GBC35 bodies on one side and MMP10-MMP20 bodies on the other (Fig. 8). The effective viscosity can decrease with increasing temperature for two reasons: the natural drop in the viscosity of the melt, but also the loss of solid load due to melting of the crystalline
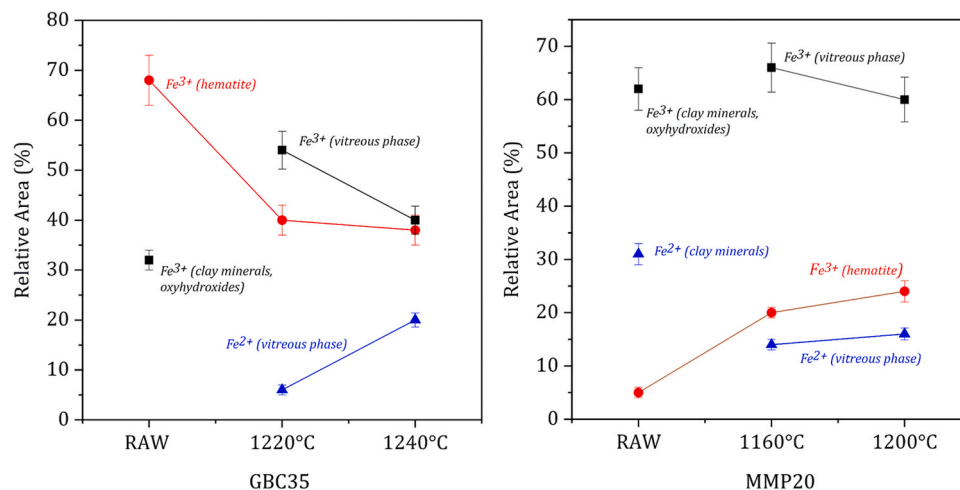

Fig. 6. Speciation of iron during the firing: change of the relative areas of the different Fe species as function of the temperature. Black squares stand for paramagnetic Fe^{3+}; blue triangles for paramagnetic Fe^{2+}, and red circles for magnetically coupled Fe^{3+} components.

Table 4

Chemical composition, calculated pseudostructural parameters and physical properties at high temperature of the amorphous phase and the bulk body (e.u. = experimental uncertainty).

|	unit	B0	GBC20	GBC35	GBC35	MMP10	MMP20	MMP20	e.u.
Optimal firing temperature	°C	1200	1220	1220	1240	1180	1160	1200	5
SiO_2	wt%	67.90	68.09	68.37	69.91	65.61	62.03	66.01	0.5
TiO_2	wt%	0.69	0.84	0.55	0.83	0.29	0.20	0.43	0.02
Al_2O_3	wt%	21.11	20.24	19.75	18.21	22.39	24.55	21.01	0.2
Fe_2O_3	wt%	1.02	1.46	1.94	1.81	1.88	3.00	2.22	0.02
MgO	wt%	0.82	0.72	0.69	0.65	1.35	1.92	1.43	0.02
CaO	wt%	1.04	0.85	0.80	0.75	1.28	1.54	1.14	0.02
Na_2O	wt%	4.98	5.51	5.58	5.66	4.21	3.49	5.32	0.05
K_2O	wt%	2.43	2.29	2.33	2.18	3.00	3.28	2.43	0.03
Alumina Saturation Index	1	1.43	1.36	1.33	1.24	1.41	1.45	1.23	0.01
NBO/T	1	0.291	0.260	0.253	0.193	0.327	0.416	0.224	0.005
Glass Network Formers	%atom	40.5	40.7	41.1	41.6	40.8	40.6	41.5	0.2
Charge Compensated$^{[IV]}Al^{3+}/Fe^{3+}$	%atom	8.2	8.1	8.0	7.9	9.1	9.8	9.3	0.2
Glass Network Modifiers	%atom	3.7	3.7	3.8	3.1	4.1	5.3	3.4	0.2
Melt surface tension	N m^{-1}	0.346	0.341	0.340	0.334	0.354	0.366	0.349	0.002
Melt shear viscosity (in log unit)	Pa s	4.94	4.72	4.64	4.59	4.79	4.55	4.50	0.03
Melt timescale	s	0.94	0.66	0.60	0.55	0.65	0.36	0.34	0.03
Bulk solid fraction	1	0.389	0.372	0.394	0.354	0.459	0.464	0.279	0.005
Bulk relative viscosity	1	4.05	3.70	4.16	3.38	6.21	6.43	2.42	0.02
Bulk effective viscosity (in log unit)	Pa s	5.48	5.22	5.18	5.07	5.46	5.23	4.86	0.03
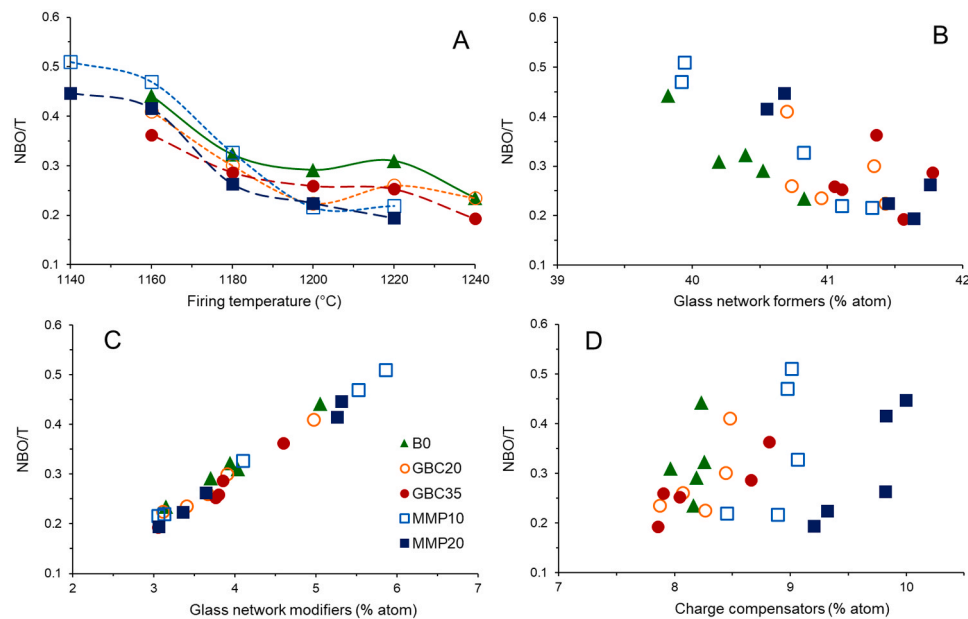
Fig. 7. Number of Non-Bridging Oxygen per Tetrahedral unit (NBO/T) in the melt as a function of firing temperature (A) and in relation to the pseudostructural parameters of the liquid phase: glass network formers (B), glass network modifiers (C) and charge compensators of Al^{3+} (and Fe^{3+}) in tetrahedral coordination (D). Experimental error is within the symbol size.

components, which determines a change in the composition of the melt with feedback on its viscosity [94]. Interestingly, if the effective viscosity values at the maximum densification temperature are compared (Table 4) it can be appreciated that the most viscous bodies are the benchmark and MMP10 (with effective viscosity about 5.5 log Pa·s) and that the remaining bodies have values close to 5.2 log Pa·s. These values are within the literature range for porcelain stoneware tiles [24,67,94]. Indeed, it seems necessary to have an effective viscosity of at least 5.2 log Pa·s to ensure adequate dimensional stability at maximum densification, irrespective of the iron content.

4.6. Sintering behaviour and microstructure of iron-rich bodies

The sintering behaviour of porcelain stoneware bodies can be followed by isothermal curves at various temperatures: the results are summarized in Table S4 (supplementary material). For the temperatures

of maximum densification, relevant data are summarized in Table 5.

The bodies under investigation exhibit different kinetics of densification at T_{md}. The sintering rate of the benchmark is apparently slower than in iron-enriched bodies, where GBC20 and GBC35 are characterized by faster kinetics than MMP10-MMP20, which T_{md} is lower. This is clearly observed for the total sintering rate and the rate in the final stage, in which sintering proceeds according to the vented bubble model. In the initial stage, which is attributed to neck formation between particles, the benchmark's densification rate was more or less the same of MMP20 (Fig. 9A).

In addition, de-densification kinetics was quantified by a bloating rate (Table 5). All iron-enriched bodies suffer from bloating rates significantly faster than the benchmark, coupled in MMP20 with the highest increase of volume (Fig. 9B). The peculiar behavior of MMP10, which is quite close to the benchmark both for sintering kinetics and bloating rate, is due to the combination of high solid load and lower melt
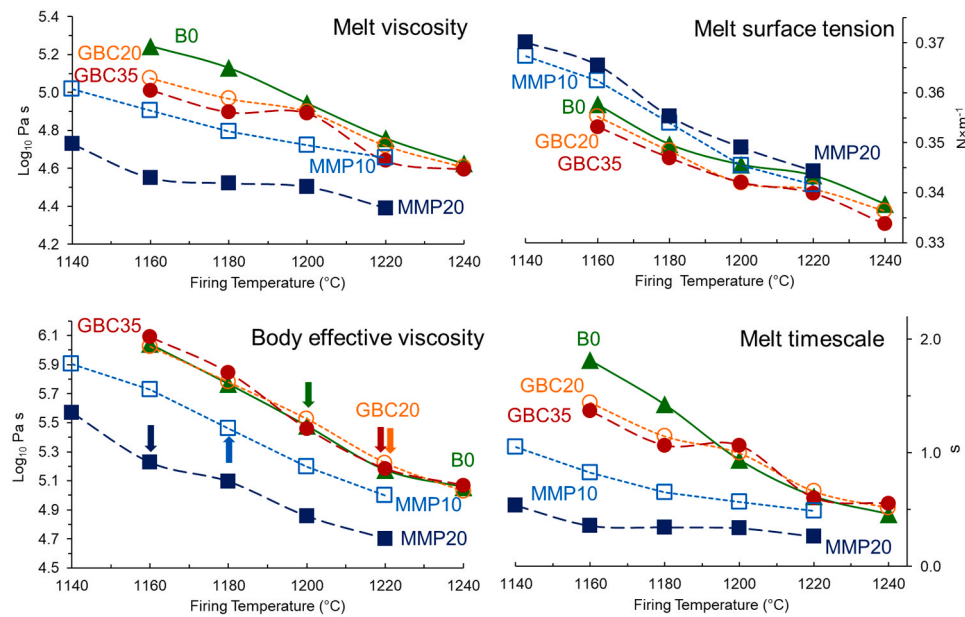
Fig. 8. Trends of calculated shear viscosity (Log_{10} Pa·s), surface tension ($N·m^{-1}$) and timescale (s) of the melt, and effective viscosity of the bulk (Log_{10} Pa·s) as a function of firing temperature (°C). Arrows indicate the temperature of maximum densification for each batch. Experimental error is within the symbol size.

Table 5

Sintering parameters of porcelain stoneware bodies at the temperature of maximum densification (e.u. = experimental uncertainty).

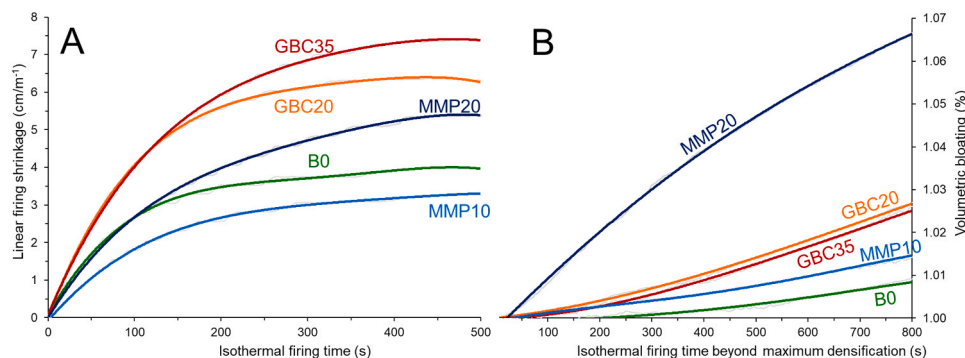|	unit	BMK	GBC20	GBC35	MMP10	MMP20	e.u.
Optimal firing temperature	°C	1200	1220	1220	1180	1160	5
Isothermal sintering rate (neck formation stage)	min^{-1}	1.97	3.13	2.73	1.30	1.85	0.03
Isothermal sintering rate (vented bubble stage)	min^{-1}	0.12	0.50	0.60	0.15	0.25	0.02
Total sintering rate	min^{-1}	0.23	0.71	0.86	0.36	0.37	0.02
Bloating rate	min^{-1}	0.0009	0.0027	0.0030	0.0015	0.0013	0.0001

Fig. 9. Isothermal runs at the temperature of maximum densification: A) sintering curves and B) bloating curves.

viscosity, so that its effective viscosity is comparable to B0.

The microstructure at maximum densification is similar in all bodies (Fig. 10). Typical microstructural features of porcelain stoneware appear, particularly the occurrence of a residual porosity, consisting of both spheroidal pores (generally under 10 μm) and irregular shapes (up to 50 μm). In addition, residual grains of quartz (dark grey), plagioclase (light grey) and Fe-Ti oxides (white) can also be observed. Microstructures clearly change at 20–40 °C above T_{md} (i.e., in overfiring conditions). In this case, spheroidal pores represent the predominant residual porosity. In the iron-rich bodies, however, the size of some spheroidal pores is markedly greater than the spheroidal pores observed at T_{md}, as they attained 40–50 μm (Fig. 10 bottom part).

The sintering kinetics became clearly faster as the firing temperature increased, but interestingly the variations occurred with a similar slope for all samples (Fig. 11A). The differences in sintering rates shown in Table 5 reflect more the different T_{md} rather than a prevailing effect of iron (or the mineralogical composition of red clays) on the firing kinetics. The sintering kinetics (determined via HSM) appear to be effectively correlated with the properties of the liquid phase (expressed as timescale), even if with different trends. The benchmark and GBC20-GBC35 bodies have the expected negative relationship between sintering rates and melt timescales (Fig. 11B). The same relationship can also be perceived for MMP10-MMP20 bodies, which nevertheless exhibit very steep sintering rate-timescale trends due to the fact they have very
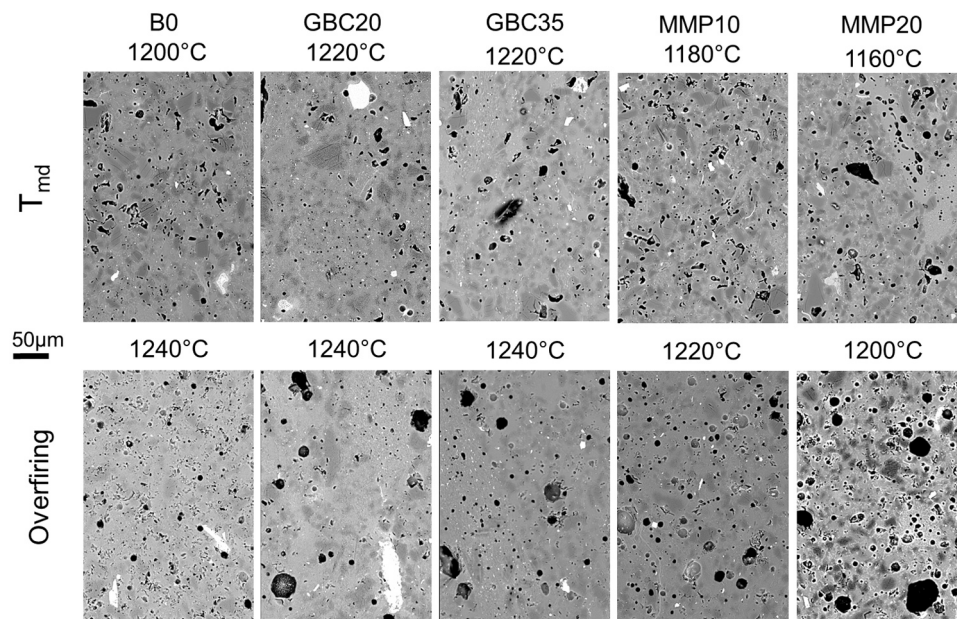
Fig. 10. SEM micrographs of porcelain stoneware tiles: microstructure of bodies fired at the temperature of maximum densification (upper figures) and in overfiring conditions (bottom figures).
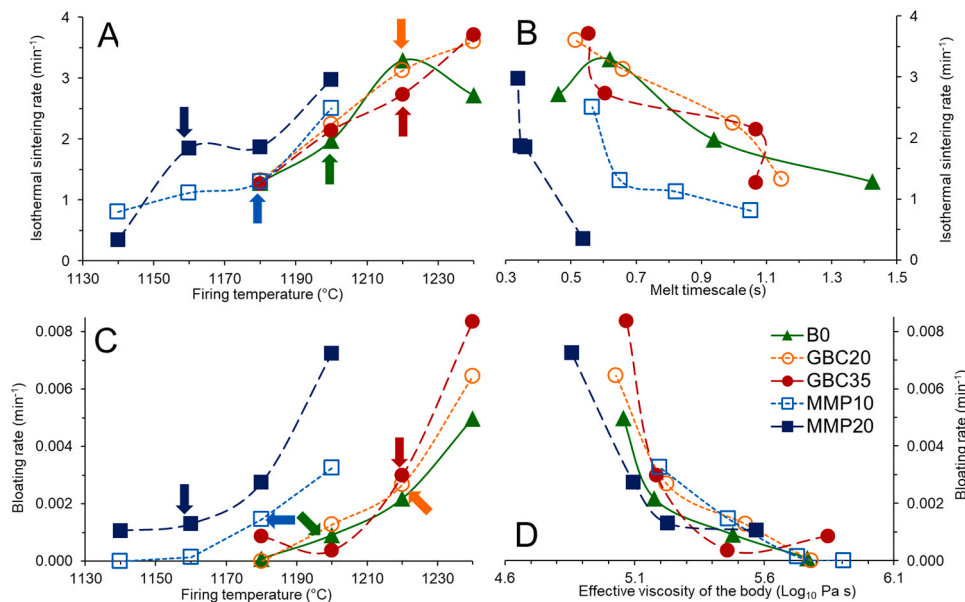

Fig. 11. Trends of isothermal sintering rate (at the neck formation stage) of porcelain stoneware bodies as a function of firing temperature (A) and melt timescale (B). Bloating rate as a function of firing temperature (C) and effective viscosity of the bulk (D). Arrows indicate the temperature of maximum densification for each batch. Experimental error is within the symbol size.

narrow variations of the physical properties as a function of temperature. It is difficult to decipher a specific role of iron in the sintering of these bodies, where the breakdown of clay minerals and carbonates led to a simultaneous enrichment of Ca, Mg and K as well as Fe.

The swelling due to overfiring occurred in the various bodies as almost parallel trends, which differ essentially by the temperature at which the bloating is triggered (Fig. 11C). GBC20-GBC35 bodies behave similarly to the benchmark, while MMP10 and MMP20 begin to bloat at lower temperatures. In the interpretation of these behaviours, it must be considered that the phenomenon of bloating can be attributed to two main causes: i) oxygen release from Fe^{3+} reduction to Fe^{2+} [26] and ii) progressive relaxation until the collapse of the material when the bulk viscosity turns too low [95]. Some iron reduction was observed in GBC35 (and to a lesser extent MMP20) when in overfiring. Nonetheless, the bloating rate is negatively correlated with the effective viscosity in the tested samples, even though in a non-linear way (Fig. 11D). This argues in favour of a dominant effect of the decrease in bulk viscosity. However, the occurrence of larger spheroidal pores in iron-rich bodies (Fig. 10) is consistent with the release of oxygen due to the reduction of Fe^{3+} at overfiring temperatures. Thus, it is likely that the two causes of bloating operate simultaneously and it is not a case that bodies are prone to overfiring in a different way. To have bodies with low bloating rate (e. g., below 0.001 min^{-1} in Fig. 11D) the effective viscosity must be at least 5.6 log Pa·s for the benchmark and GBC20-GBC35. At variance, effective viscosity values as low as 5.2 log Pa·s are tolerated in MMP10 and MMP20 bodies.

5. Conclusions

The effect of relatively high iron content on the firing behaviour of porcelain stoneware tiles must be assessed together with the overall mineralogical and chemical composition of the batch, resulting from the introduction of iron-rich raw materials. In the present study, the behaviour of porcelain stoneware was investigated with excess iron brought by the clay component. Further work is required to assess the effect of other iron-rich components in order to gain a general framework.

The kinetics of phase transformations during firing are not substantially modified by the occurrence of higher amounts of iron oxide in the body. However, the use of red clays, with mineralogical composition differing from conventional ball clays, had a clear impact on both vitrification paths and temperature at which the maximum densification was achieved. This in turn affected the phase composition and the chemical composition of the vitreous phase at the optimal firing temperature (richer in alkali and alkali-earths as well as iron). As the firing temperature increased, the liquid phase became progressively more polymerized and less peraluminous. The glass network modifiers are basically represented by aluminium and iron in all bodies.

The firing transformations of Fe-bearing minerals consisted mainly in the formation of hematite (at expenses of Fe-oxyhydroxides) and incorporation in the liquid phase of iron made available by the breakdown of clay minerals. There was a general tendency to stabilize Fe^{3+}, with partial oxidation of Fe^{2+} originally present in clay minerals, up to the temperature of maximum densification. When the temperature was increased to overfiring conditions, a partial reduction to Fe^{2+} occurred up to a $Fe^{3+}/Fe_{total} \sim 0.8$ (which approximates the expected value at temperature, pressure and oxygen fugacity of ceramic kilns).

Viscosity decreased faster than surface tension as temperature increased, resulting in a faster timescale of the melts. The effect of iron on viscosity appears to be less pronounced than variations in the chemical composition of the melts: the silica content, which characterized the benchmark and GBC20-GBC35 bodies, and the contextual increasing of MgO and CaO in MMP10-MMP20 bodies.

The densification kinetics of the bodies followed fairly well the timescale calculated for the liquid phase in the case of benchmark and more siliceous mixtures (GBC20-GBC35). The same relationship also applies to less siliceous batches (MMP10-MMP20) although the variations of melt timescale with firing temperature are much narrower.

Bodies exhibited different bloating rates, which can be attributed to two coexisting causes: excessive loss of bulk viscosity (due to melting of crystalline phases) or release of oxygen (by reducing Fe^{3+} to Fe^{2+}). The effective viscosity change appears to be the dominant driving force of bloating, although there is microstructural evidence of a possible contribution by the gas release.

Declaration of Competing Interest

The authors declare that they have no known competing financial interests or personal relationships that could have appeared to influence the work reported in this paper.

Acknowledgements

Appendix A. Supporting information

Supplementary data associated with this article can be found in the online version at doi:10.1016/j.jeurceramsoc.2024.116947.

References

[1] M. Dondi, G. Ercolani, C. Melandri, C. Mingazzini, M. Marsigli, The chemical composition of porcelain stoneware tiles and its influence on microstructural and mechanical properties, Interceram 48 (2) (1999) 75–83.

[2] E. Sánchez, J. García-Ten, V. Sanz, A. Moreno, Porcelain tile: almost 30 years of steady scientific-technological evolution, Ceram. Int. 36 (3) (2010) 831–845.

[3] P. de Oliveira Piccolo, A. Zaccaron, L.B. Teixeira, E.G. de Moraes, O.R.K. Montedo, A.P.N. de Oliveira, Development of translucent ceramic tiles from modified porcelain stoneware tile paste, J. Build. Eng. 45 (2022) 103543, https://doi.org/10.1016/j.jobe.2021.103543.

[4] A. Salem, S.H. Jazayeri, E. Rastelli, G. Timellini, Effect of nepheline syenite on the colorant behavior of porcelain stoneware body, J. Ceram. Process. Res. 10 (5) (2009) 621–627.

[5] K. Wiśniewska, E. Kłosek-Wawrzyn, R. Lach, W. Pichór, Influence of the grain size distribution of the limestone additives on the color properties and phase composition of sintered ceramic materials based on cream-firing clays, Materials 15 (7) (2022) 2694.

[6] A. De Noni Junior, S.B. Canever, P. Henrique, R.R. da Silva, Microstructure-oriented porcelain stoneware tile composition design, Ceram. Int. 49 (14) (2023) 24558–24565.

[7] Conte, S., Molinari, C., Javed, S., Dondi, M., & Zanelli, C. (2024). Compositional Diversity of Vitrified Silicate Ceramics: Delimiting the Chemical Perimeter of Industrial Bodies. Ceramics International, in press, https://doi.org/10.1016/j.ceramint.2024.09.024.

[8] E. Rambaldi, Pathway towards a high recycling content in traditional ceramics, Ceramics 4 (3) (2021) 486–501.

[9] M. Dondi, J. García-Ten, E. Rambaldi, C. Zanelli, M. Vicent-Cabedo, Resource efficiency versus market trends in the ceramic tile industry: Effect on the supply chain in Italy and Spain, Resour., Conserv. Recycl. 168 (2021) 105271.

[10] A.E. Benlloch, J.A. Albaro, J.E. Navarro, Estudio de pastas de gres para pavimentos, BoletíN. De. la Soc. Española De. Cerámica Y. Vidr. 20 (1) (1981) 17–24.

[11] C. Fiori, B. Fabbri, G. Donati, I. Venturi, Mineralogical composition of the clay bodies used in the Italian tile industry, Appl. Clay Sci. 4 (5-6) (1989) 461–473.

[12] S.R. Christofoletti, A. Batezelli, M.M.T. Moreno, Facies, geochemistry, and ceramic properties of corumbataí formation, upper permian of paraná basin, and its application in the ceramic industry, Brazil. Clays Clay Miner. 70 (5) (2022) 712–732.

[13] N. Nawaukkaratharnant, A. Thueploy, S. Khunthon, S. Nilpairach, A. Theerapapvisetpong, Improving the technological properties of red stoneware tiles derived from Ratchaburi red clay by the addition of iron oxide, Case Stud. Constr. Mater. 16 (2022) e00983.

[14] M. Dondi, M. Raimondo, C. Zanelli, Clays and bodies for ceramic tiles: reappraisal and technological classification, Appl. Clay Sci. 96 (2014) 91–109.

[15] G. Ferrari, P. Zannini, C. Baraldi, Study of Black Core, ceramic tile's defect, by a multi technique approach. ICORS 2014-XXIV Int. Congr. Raman Spectrosc. Proc. (2014).

[16] S. Chorlet, Eliminación del fenómeno de corazón negro en los ciclos de cocción rápida. Boletín de la Sociedad Española, De. Cerámica Y. Vidr. 33 (3) (1994) 149–150.

[17] L.R. dos Santos Conserva, F.G. Melchiades, S. Nastri, A.O. Boschi, M. Dondi, G. Guarini, C. Zanelli, Pyroplastic deformation of porcelain stoneware tiles: Wet vs. dry processing, J. Eur. Ceram. Soc. 37 (1) (2017) 333–342.

[18] E. Sánchez, V. Sanz, E. Cañas, J. Sales, K. Kayacı, M.U. Taşkıran, Ş. Türk, Revisiting pyroplastic deformation. Application for porcelain stoneware tile bodies, J. Eur. Ceram. Soc. 39 (2-3) (2019) 601–609.

[19] C.T. Brasileiro, S. Conte, F. Contartesi, F.G. Melchiades, C. Zanelli, M. Dondi, A. O. Boschi, Effect of strong mineral fluxes on sintering of porcelain stoneware tiles, J. Eur. Ceram. Soc. 41 (11) (2021) 5755–5767.

[20] R. Fantini, S. Conte, A.F. Gualtieri, M. Dondi, F. Colombo, M. Sisti, C. Molinari, C. Zanelli, R. Arletti, Reappraisal of red clays in porcelain stoneware production: compositional and technological characterization, Appl. Clay Sci. 250 (2024) 107291.

[21] S. Conte, C. Zanelli, M. Ardit, G. Cruciani, M. Dondi, Phase evolution during reactive sintering by viscous flow: Disclosing the inner workings in porcelain stoneware firing, J. Eur. Ceram. Soc. 40 (4) (2020) 1738–1752.

[22] J.L. Amorós, E. Blasco, A. Moreno, C. Feliu, Kinetics of the transformations occurring during the firing process of an industrial spray-dried porcelain stoneware body, Ceram. Int. 48 (12) (2022) 17611–17620.

[23] C. Zanelli, M. Raimondo, G. Guarini, M. Dondi, The vitreous phase of porcelain stoneware: composition, evolution during sintering and physical properties, J. Non-Cryst. Solids 357 (16-17) (2011) 3251–3260.

[24] S. Conte, C. Molinari, M. Ardit, G. Cruciani, M. Dondi, C. Zanelli, Porcelain versus porcelain stoneware: so close, so different. Sintering kinetics. Phase evolution, and vitrification paths, Materials 16 (2023) 171.

[25] B.O. Mysen, D. Virgo, E.R. Neumann, F.A. Seifert, Redox equilibria and the structural states of ferric and ferrous iron in melts in the system CaO–MgO–Al2O3–SiO2–Fe–O: relationships between redox equilibria, melt structure and liquidus phase equilibria. Am. Mineral. 70 (3-4) (1985) 317–331.

[26] V.C. Kress, I.S. Carmichael, Stoichiometry of the iron oxidation reaction in silicate melts, Am. Mineral. 73 (11-12) (1988) 1267–1274.

[27] B.O. Mysen, D. Virgo, Redox equilibria, structure, and properties of Fe-bearing aluminosilicate melts; relationships among temperature, composition, and oxygen fugacity in the system Na_2O-Al_2O_3-SiO_2-Fe-O, Am. Mineral. 74 (1-2) (1989) 58–76.

[28] M.V. Volovetskii, O.A. Lukanin, V.S. Rusakov, A.A. Kargal'tsev, Influence of oxygen fugacity and temperature on the redox state of iron in natural silicic aluminosilicate melts, Geochem. Int. 50 (2012) 330–343.

[29] P. Stabile, G. Giuli, M.R. Cicconi, E. Paris, A. Trapananti, H. Behrens, The effect of oxygen fugacity and Na/(Na+ K) ratio on iron speciation in pantelleritic glasses. J. Non-Cryst. Solids 478 (2017) 65–74.

[30] Mysen, B., & Richet, P. (2018). Silicate glasses and melts. Elsevier.

[31] R. Moretti, G. Ottonello, Silicate melt thermochemistry and the redox state of magmas, Rev. Mineral. Geochem. 87 (1) (2022) 339–403.

[32] D. González-García, D. Giordano, J.K. Russell, Donald B. Dingwell, A Raman spectroscopic tool to estimate chemical composition of natural volcanic glasses, Chem. Geol. 556 (2020) 119819, https://doi.org/10.1016/j.chemgeo.2020.119819.

[33] F. Radica, M. Cassetta, G. Iezzi, A. Pisello, F. Vetere, A. Del Vecchio, B.T. Poe, Short-range order and chemical compositions of glasses along the basaltic-rhyolite sub-alkaline join by Raman and FTIR spectroscopies, Chem. Geol. 648 (2024) 121938.

[34] D. Virgo, B.O. Mysen, The structural state of iron in oxidized vs. reduced glasses at 1 atm: A 57Fe Mössbauer study, Phys. Chem. Miner. 12 (2) (1985) 65–76.

[35] E. Antoni, L. Montagne, S. Daviero, G. Palavit, J.L. Bernard, A. Wattiaux, H. Vezin, Structural characterization of iron–alumino–silicate glasses. J. Non-Cryst. Solids 345 (2004) 66–69.

[36] B.O. Mysen, The structural behavior of ferric and ferrous iron in aluminosilicate glass near meta-aluminosilicate joins, Geochim. Et. Cosmochim. Acta 70 (9) (2006) 2337–2353.

[37] A. Di Muro, N. Metrich, M. Mercier, D. Giordano, M. Massarre, G. Montagnac, MicroRaman Determination of Iron Redox State in Dry Natural Glasses: Application to Peralkaline Rhyolites and Basalts, Chem. Geol. 259 (2009) 78–88.

[38] M. Mercier, A. Di Muro, D. Giordano, N. Métrich, P. Lesne, M. Pichavant, B. Scaillet, R. Clocchiatti, G. Montagnac, Influence of glass polymerisation and oxidation on micro-Raman water analysis in alumino-silicate glasses, Geochim. Cosmochim. Acta 73 (2009) 197–217.

[39] M. Mercier, A. Di Muro, N. Métrich, D. Giordano, O. Belhadj, C.W. Mandeville, Spectroscopic analysis (FTIR, Raman) of water in mafic and intermediate glasses and glass inclusions, Geochim. Cosmochim. Acta 74 (2010) 5641–5656.

[40] N.O. Dantas, W.E. Ayta, A.C. Silva, N.F. Cano, S.W. Silva, P.C. Morais, Effect of Fe2O3 concentration on the structure of the SiO2–Na2O–Al2O3–B2O3 glass system. Spectrochim. Acta Part A: Mol. Biomol. Spectrosc. 81 (1) (2011) 140–143.

[41] H.I. Kim, S.K. Lee, Extent of disorder in iron-bearing albite and anorthite melts: Insights from multi-nuclear (29Si, 27Al, and 17O) solid-state NMR study of iron-bearing NaAlSi3O8 and CaAl2Si2O8 glasses, Chem. Geol. 538 (2020) 119498.

[42] C. Le Losq, M.R. Cicconi, D.R. Neuville, Iron in silicate glasses and melts: implications forvolcanological processes, Magma Redox Geochem. (2021) 233–253.

[43] Cassetta, M., De Bona, E., Sambugaro, A., Enrichi, F., Daldosso, N., Giannetta, B., Biesuz, M., Sglavo, V., Almeev, R., Nodari, L., Giordano, D., Mariotto, G. (2024). Fe-dependent structural evolution of peralkaline silicate glasses: iron speciation vs. glass transition. Submitted2024, , ..

[44] D.B. Dingwell, D. Virgo, The effect of oxidation state on the viscosity of melts in the system Na2O-FeO-Fe2O3-SiO2, Geochim. Et. Cosmochim. Acta 51 (2) (1987) 195–205.

[45] D.B. Dingwell, D. Virgo, Viscosities of melts in the Na2O-FeO-Fe2O3-SiO2 system and factors controlling relative viscosities of fully polymerized silicate melts, Geochim. Et. Cosmochim. Acta 52 (2) (1988) 395–403.

[46] D.B. Dingwell, Redox viscometry of some Fe-bearing silicate melts, Am. Mineral. 76 (9-10) (1991) 1560–1562.

[47] D. Giordano, A. Mangiacapra, M. Potuzak, J.K. Russell, C. Romano, D.B. Dingwell, A. Di Muro, An expanded non-Arrhenian model for silicate melt viscosity: A treatment for metaluminous, peraluminous and peralkaline liquids, Chem. Geol. 229 (1-3) (2006) 42–56.

[48] M.O. Chevrel, D. Giordano, M. Potuzak, P. Courtial, D.B. Dingwell, Physical properties of CaAl2Si2O8 - CaMgSi2O6 - FeO - Fe2O3 melts: Analogues for extra-terrestrial basalt, Chem. Geol. 346 (2013) 93–105.

[49] P. Stabile, S. Webb, J.L. Knipping, H. Behrens, E. Paris, G. Giuli, Viscosity of pantelleritic and alkali-silicate melts: Effect of Fe redox state and Na/(Na+ K) ratio, Chem. Geol. 442 (2016) 73–82.

[50] Y. Shaharyar, J.Y. Cheng, E. Han, A. Maron, J. Weaver, J. Marcial, A. Goel, Elucidating the effect of iron speciation (Fe^{2+}/Fe^{3+}) on crystallization kinetics of sodium aluminosilicate glasses, J. Am. Ceram. Soc. 99 (7) (2016) 2306–2315.

[51] D. Di Genova, J. Vasseur, K.U. Hess, D.R. Neuville, D.B. Dingwell, Effect of oxygen fugacity on the glass transition, viscosity and structure of silica-and iron-rich magmatic melts, J. Non-Cryst. Solids 470 (2017) 78–85.

[52] S. Kolzenburg, D. Di Genova, D. Giordano, K.U. Hess, D.B. Dingwell, The effect of oxygen fugacity on the rheological evolution of crystallizing basaltic melts, Earth Planet. Sci. Lett. 487 (2018) 21–32.

[53] C. Kleest, S.L. Webb, Influence of Fe2+/Fetot on the viscosity of melts from the Colli Albani Volcanic District (Italy) – foidite to phonolite, J. Vollcanol. Geoth. Res. 431 (2022) 107649.

[54] A. Borisov, H. Behrens, F. Holtz, Ferric/ferrous ratio in silicate melts: a new model for 1 atm data with special emphasis on the effects of melt composition, Contrib. Mineral. Petrol. 173 (2018) 1–15.

[55] F. Holtz, W. Johannes, M. Pichavant, Peraluminous granites: the effect of alumina on melt composition and coexisting minerals, Earth Environ. Sci. Trans. R. Soc. Edinb. 83 (1-2) (1992) 409–416.

[56] M.P. Dickenson, P.C. Hess, Redox equilibria and the structural role of iron in alumino-silicate melts, Contrib. Mineral. Petrol. 78 (1982) 352–357.

[57] A. Borisov, H. Behrens, F. Holtz, Effects of strong network modifiers on Fe3+/Fe2+ in silicate melts: an experimental study, Contrib. Mineral. Petrol. 172 (2017) 1–14.

[58] C. Rüssel, A. Wiedenroth, The effect of glass composition on the thermodynamics of the Fe2+/Fe3+ equilibrium and the iron diffusivity in Na2O/MgO/CaO/Al2O3/SiO2 melts, Chem. Geol. 213 (1-3) (2004) 125–135.

[59] J.M. Moreno-Maroto, B. González-Corrochano, A.M. Martínez-Rodríguez, A. Conde-Sánchez, C.J. Cobo-Ceacero, J. Alonso-Azcárate, T. Cotes-Palomino, Analyzing the role of Fe0 and Fe3+ in the formation of expanded clay aggregates. Materials 16 (16) (2023) 5623.

[60] M. Franzini, L. Leoni, M. Saitta, Revisione di una metodologia analitica per fluorescenza-X, basata sulla correzione completa degli effetti di matrice, Rend. Soc. Ital. Mineral. Petrol. 31 (1975) 365–378.

[61] L. Leoni, M. Saitta, X-ray fluorescence analysis of 29 trace elements in rock and mineral standards, Rend. Soc. Ital. Mineral. Petrol. 32 (1976) 497–519.

[62] A.F. Gualtieri, V. Riva, A. Bresciani, S. Maretti, M. Tamburini, A. Viani, Accuracy in quantitative phase analysis of mixtures with large amorphous contents. The case of stoneware ceramics and bricks, J. Appl. Crystallogr. 47 (3) (2014) 835–846.

[63] N. Doebelin, R. Kleeberg, Profex: a graphical user interface for the Rietveld refinement program BGMN, J. Appl. Crystallogr. 48 (2015) 1573–1580, https://doi.org/10.1107/S1600576715014685.

[64] B.H. Toby, EXPGUI, A graphical user interface for GSAS, J. Appl. Crystallogr. 34 (2001) 210–213.

[65] Larson, A.C., Von Dreele, R.B., (1994). General structure analysis system "GSAS". Los Alamos National Laboratory Report, Los Alamos, LAUR 86-748.

[66] G.S. Prata, L.J. Ventress, E. Carboni, T.A. Mather, R.G. Grainger, D.M. Pyle, A new parameterization of volcanic ash complex refractive index based on NBO/T and SiO2 content, J. Geophys. Res.: Atmosph. 124 (2019) 1779–1797, https://doi.org/10.1029/2018JD028679.

[67] S. Conte, C. Zanelli, C. Molinari, G. Guarini, M. Dondi, Glassy wastes as feldspar substitutes in porcelain stoneware tiles: thermal behaviour and effect on sintering process, Mater. Chem. Phys. 256 (2020) 123613.

[68] D. Giordano, J.K. Russell, D.B. Dingwell, Viscosity of magmatic liquids: a model, Earth Planet. Sci. Lett. 271 (1-4) (2008) 123–134.

[69] A.A. Appen, Chemistry of Glass, Khimiya, Saint Petersburg, Russia, 1974, p. 351.

[70] A. Dietzel, Relation between the surface tension and the structure of molten glass, Kolloid-Z. 100 (1942) 368–380.

[71] J. Vasseur, F.B. Wadsworth, Y. Lavallee, K.U. Hess, D.B. Dingwell, Volcanic sintering: timescales of viscous densificationand strength recovery, Geophys. Res. Lett. 40 (2013) 5658–5664.

[72] A. Costa, L. Caricchi, N. Bagdassarov, A model for the rheology of particle-bearing suspensions and partially molten rocks, Geochem. Geophys. 10 (2009) 1–13.

[73] A.E. Lalonde, D.G. Rancourt, J.Y. Ping, Accuracy of ferric/ferrous determinations in micas: a comparison of Mössbauer spectroscopy and the Pratt and Wilson wet-chemical methods, Hyperfine Inter. 117 (1998) 175–204.

[74] D.G. Rancourt, J.Y. Ping, Voigt-based methods for arbitrary shape static hyperfine parameter distributions in Mössbauer spectroscopy, Nucl. Instrum. Methods Phys. Res B 58 (1991) 85–97, https://doi.org/10.1016/0168-583X(91)95681-3.

[75] M.G. Ferreira da Silva, B.F.O. Costa, Infrared and Mössbauer studies of iron in aluminosilicate glasses, J. Non-Cryst. Solids 293-295 (2001) 534–538.

[76] E. Murad, Clays and clay minerals: What can Mössbauer spectroscopy do to help understand them? Hyperfine Interact. 117 (1998) 39–70, https://doi.org/10.1023/A:1012635124874.

[77] O. Castelein, L. Aldon, J. Olivier-Fourcade, J.C. Jumas, J.P. Bonnet, P. Blanchart, 57Fe Mössbauer study of iron distribution in a kaolin raw material: influence of the temperature and the heating rate, J. Eur. Ceram. Soc. 22 (2002) 1767–1773, https://doi.org/10.1016/S0955-2219(01)00496-4.

[78] E. Murad, U. Wagner, The Mössbauer Spectrum of Illite, Clay Miner. 29 (1994) 1–10, https://doi.org/10.1180/claymin.1994.029.1.01.

[79] M. Darby Dyar, Optical and mössbauer spectroscopy of iron in micas. Rev. Mineral. Geochem. 46 (1) (2002) 313–349, https://doi.org/10.2138/rmg.2002.46.06.

[80] E. Murad, Mössbauer spectroscopy of clays, soils and their mineral constituents, Clay Miner. 45 (4) (2010) 413–430, https://doi.org/10.1180/claymin.2010.045.4.413.

[81] L. Heller-Kallai, I. Rozenson, The use of Mössbauer spectroscopy of iron in clay mineralogy, Phys. Chem. Miner. 7 (1981) 223–238, https://doi.org/10.1007/BF00311893.

[82] Gómez-Tena, M.P., Gilabert, J. Zumaquero, E., Díaz-Canales, E.M., Arrufat, S., Domínguez, R. (2024). Reactivity of crystalline silica in processing ceramic tiles. Proceedings of the18th World Congress on Ceramic Tile Quality, QUALICER2024, Castellón (Spain), 5-6 March, 14 pages.

[83] C. Tavares Brasileiro, H.D. de Almeida Filho, G.L. Santana, A.V. Lot, S. Conte, C. Zanelli, M. Dondi, A. Ortega Boschi, Sericite instead of feldspar in porcelain stoneware: effect on sintering and phase evolution, Int. J. Appl. Ceram. Technol. 19 (1) (2022) 612–622.

[84] J. Martín-Márquez, J.M. Rincón, M. Romero, Mullite development on firing in porcelain stoneware bodies, J. Eur. Ceram. Soc. 30 (7) (2010) 1599–1607.

[85] M. Lassinantti Gualtieri, M. Romagnoli, A.F. Gualtieri, Influence of body composition on the technological properties and mineralogy of stoneware: A DOE and mineralogical–microstructural study, J. Eur. Ceram. Soc. 31 (5) (2011) 673–685.

[86] F.M. Brasil, D.L. Oliveira, M.O. Melquíades, F.X. Nobre, C.E.T. Balestra, J. D. Ardisson, J.D. Fabris, G.P. Santana, M.A. Ramirez, Influence of kaolin and red clay on ceramic specimen properties when galvanic sludge is incorporated to encapsulate heavy metals, Waste Manag. 181 (2024) 176–187.

[87] R.E. Vandenberghe, E. Van San, E. De Grave, G.M. da Costa, About the Morin transition in hematite in relation with particle size and aluminum substitution, Czechoslov. J. Phys. 51 (2001) 663–675.

[88] N. Soro, L. Aldon, J. Olivier-Fourcade, J.C. Jumas, J.P. Laval, P. Blanchart, Role of iron in mullite formation from kaolins by mössbauer spectroscopy and rietveld refinement, J. Am. Ceram. Soc. 86 (2003) 129–134, https://doi.org/10.1111/j.1151-2916.2003.tb03289.x.

[89] M.T. Nayak, J.A.E. Desa, V.R. Reddy, C. Nayak, D. Bhattacharyya, S.N. Jha, Structural studies of potassium silicate glasses with fixed iron content and their relation to similar alkali silicates, J. Non-Cryst. Solids 518 (2019) 85–91, https://doi.org/10.1016/j.jnoncrysol.2019.04.025.

[90] W.E. Jackson, F. Farges, M. Yeager, P.A. Mabrouk, S. Rossano, G.A. Waychunas, E. I. Solomon, G.E. Brown, Multi-spectroscopic study of Fe(II) in silicate glasses: implications for the coordination environment of Fe(II) in silicate melts, Geochim. Et. Cosmochim. Acta 69 (17) (2005) 4315–4332, https://doi.org/10.1016/j.gca.2005.01.008.

[91] M. Cassetta, F. Vetere, M. Zanatta, D. Perugini, M. Alvaro, B. Giannetta, C. Zaccone, N. Daldosso, Micro-Raman spectroscopy for a comprehensive understanding of the structural evolution of Basaltic-Andesite and Trachybasalt multiphase systems, Chem. Geol. 616 (2023) 121241.

[92] B. Spiering, F.A. Seifert, Iron in silicate glasses of granitic composition: a Mössbauer spectroscopic study, Contr. Mineral. Petrol. 90 (1985) 63–73, https://doi.org/10.1007/BF00373042.

[93] M. Cassetta, B. Giannetta, F. Enrichi, C. Zaccone, G. Mariotto, M. Giarola, L. Nodari, M. Zanatta, N. Daldosso, Effect of the alkali vs. iron ratio on glass transition temperature and vibrational properties of synthetic basalt-like glasses, Spectrochim. Acta - Part A Mol. Biomol. Spectrosc. 293 (2023) 122430.

[94] S. Conte, C. Zanelli, M. Ardit, G. Cruciani, M. Dondi, Predicting viscosity and surface tension at high temperature of porcelain stoneware bodies: a methodological approach, Materials 11 (12) (2018) 2475.

[95] D. Giordano, Advances in the rheology of natural multiphase silicate melts: importance for magma transport and lava flow emplacement, Ann. Geophys. 61 (2019) 1–6.